



Electrical and optical characterization of Os-substituted rare-earth orthoferrite $\text{YbFeO}_{3-\gamma}$ powders

O. Polat^{1,2} · M. Coskun³ · D. Sobola^{1,4} · B. Zengin Kurt⁵ · M. Caglar⁶ · A. Turut³

Received: 28 October 2020 / Accepted: 1 December 2020 / Published online: 2 January 2021
© The Author(s), under exclusive licence to Springer-Verlag GmbH, DE part of Springer Nature 2021

Abstract

The electrical properties of Os-doped YbFeO_3 (YbFO) powders prepared by solid-state reaction have been studied by Impedance Spectrometer/Impedance Spectrometer. SEM, XPS and Raman spectroscopy were utilized for understanding chemical and structured analysis of the synthesized compounds. SEM images have revealed the void nature of the pellets. Furthermore, XPS studies have exhibited that Yb has 3+ valance state. It is also revealed that the oxygen vacancies concentration drops as the Os doping level raises by XPS analysis. The frequency dependency of loss-tan(δ) examination has demonstrated that the 5 mol% Os-substituted sample has the lowest loss-tan(δ) values at high frequency regions at 100 °C. It has been also realized that the 5 mol% Os-doped compound exhibits the highest resistivity among the samples. Raman spectroscopy examination has unveiled that the samples have similar space group. In addition, the optical band gap of the synthesized powders was also extracted via utilizing the Kubelka–Munk technique. It was realized that the band gap of YbFO slightly increases as the Os dopant ratio advances.

Keywords Solid-state reaction · Os substitution · Electrical properties · Raman spectroscopy · Optical bandgap

1 Introduction

Rare-earth orthoferrite, RFeO_3 (R = rare earth component), materials display novel electrical, optical and magnetic features and as a result of that they find different application areas in energy storage, spintronics, optical sensors and

optical communications [1, 2]. Furthermore, it has been shown that some of rare earth orthoferrites can exhibit both magnetic and ferroelectricity properties together, which make these materials new candidates in the multiferroic applications [3–6]. In RFeO_3 structure, the bigger R cation is situated at the corner of unit cell, and Fe cations are placed at the center of octahedron FeO_6 [7]. These materials display an orthorhombic structure with a space group of Pbnm. YbFeO_3 (YbFO) belongs to rare-earth orthoferrites. Even though YbFO has orthorhombic structure, it is thin-film form can have hexagonal phase, too [8, 9]. Even though the magnetic properties of YbFO thin films have been extensively inspected, the electrical features of the same material have not attracted the same attention from the scientific community [10–12]. There are several groups including us have examined the electrical properties of YbFO material in ceramic form [13–16]. In addition, we have documented how the dopant affects the optical properties of YbFO thin films [17, 18]. Our studies have shown that the electrical and optical properties of the parental compound significantly influenced by oxidation state of the dopant, which determines the ionic radius. Because the dopant initiates crystal distortions and charge imbalance in the parent sample.

✉ O. Polat
ozgur.polat@ceitec.vutbr.cz; ozgurpolat7@gmail.com

¹ CEITEC BUT, Brno University of Technology, Purkyňova 123, 612 00 Brno, Czech Republic

² Institute of Physical Engineering, Brno University of Technology, Technická 2, 616 69 Brno, Czech Republic

³ Department of Engineering Physics, Faculty of Engineering and Natural Sciences, Istanbul Medeniyet University, Uskudar, 34700 İstanbul, Turkey

⁴ Department of Physics, Faculty of Electrical Engineering and Communication, Brno University of Technology, Technická 2848/8, 616 00 Brno, Czech Republic

⁵ Department of Pharmaceutical Chemistry, Faculty of Pharmacy, Bezmialem Vakif University, Fatih, 34093 İstanbul, Turkey

⁶ Department of Physics, Faculty of Science, Eskisehir Technical University, 26000 Eskişehir, Turkey

The present study is following up our previous study in which we have detailed the conductivity, electrical modulus, and dielectric constants of the undoped and Os-doped YbFO powders [15]. In this manuscript, our objectives are to explore (i) loss-tan(δ), (ii) impedance, (iii) resistivity versus frequency at various temperatures, (iv) Raman spectra, and (v) the optical band gap of the synthesized samples. The mentioned electrical properties have detailed because (1) the loss-tangent (dielectric loss-tangent), tan δ , is a parameter of a dielectric material that quantifies its inherent dissipation of electromagnetic energy at different frequencies. It exhibits the loss of electrical energy in the material via applied frequencies. On the other hand, the impedance spectroscopy is utilized to differentiate between transport characteristics of grains and grain boundaries in the material. In addition, the impedance spectroscopy is exploited to seek the electrical response of different phases and the dynamic behavior of localized and mobile charges in the bulk and interfacial regions in the samples. Consequently, the performance of grains, grain boundaries, electrode effects, different crystallographic entities and magnetic clusters can be investigated. It should also be mentioned that the Raman spectroscopy and optical band gap of the Os-doped YbFO powders are introduced to the scientific community by the present investigation the first time. YbFO and Os-doped YbFO powders

have been obtained by well-known solid-state reaction method. X-ray photoelectron spectroscopy (XPS), scanning electron microscopy (SEM), Raman spectroscopy method were utilized to seek the chemical and structural analyses of the fabricated powders. Moreover, the electrical features of the compounds were studied with employing Broadband Dielectric/Impedance Spectrometer (Novocontrol Concept 50). Furthermore, the optical band gap undoped and Os-doped YbFO powders have been discussed in the present study.

2 Experimental

The powder preparation was discussed in our previous study [15]. The microstructure of fabricated powders was studied by ULTRAPLUS ZEISS scanning electron microscope (SEM). Furthermore, X-ray photoelectron spectroscopy (XPS) (SPECS) was utilized to seek elemental composition of powders. For the calibration purpose, the C 1s peak at 284.6 eV peak was selected. To measure the electrical properties of synthesized compounds, their pellets were prepared by applying 10 tons of pressure with 13 mm diameter and sintering during four hours at 1150 °C in the atmospheric ambient. The thickness of the pellets is of 0.91 mm,

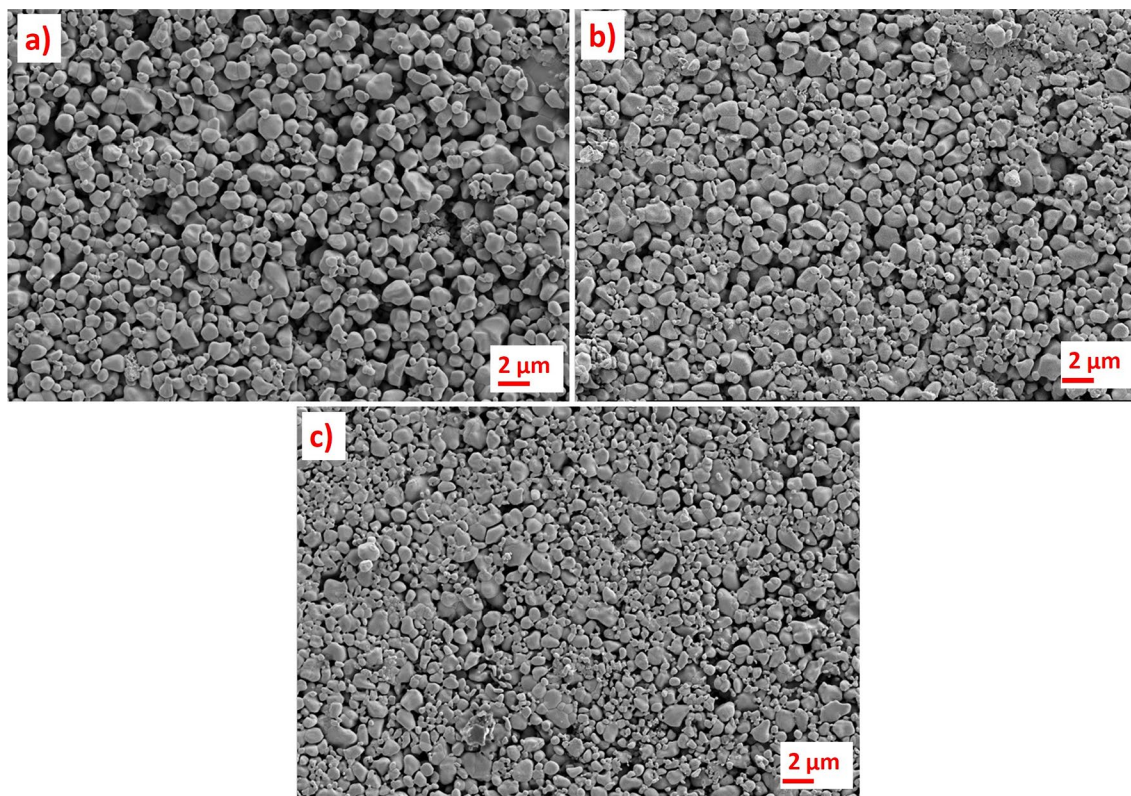


Fig. 1 SEM images of the examined samples: **a** the undoped YbFO, **b** 1% Os and **c** 5% Os-doped YbFO, respectively

1.03 mm and 0.88 mm for the undoped, 1% Os and 5% Os-doped samples, respectively. The electrical characterizations of the pellets were performed using platinum (Pt) electrode (5 mm diameter). Broadband Dielectric/Impedance Spectrometer (Novocontrol Concept 50) was exploited for the electrical properties' investigations. The operating temperature gradually was varied from $-100\text{ }^{\circ}\text{C}$ up to $100\text{ }^{\circ}\text{C}$ and the applied frequency was swept from 1 Hz up to 10 MHz. Furthermore, WITec confocal Raman imaging system was used for collecting Raman spectra at room temperature. Laser with 532 nm excitation wavelength and 5 mW power was used at integration time of 10 s. The optical band gaps of the fabricated films were investigated by UV-VIS Optical Spectrometer Ocean Optics JAZ 3-channel.

3 Results and discussion

3.1 SEM and XPS analysis

In our previous study, we have shown that the samples are single-phase with orthorhombic structure. In addition, we have not observed the formation of other phases.

Furthermore, it has been exhibited that the lattice parameters of parent compound YbFeO_3 increase as the Os dopant ratio raises, which is underlining the incorporation of Os into synthesized samples. The more detail about the crystal structure of undoped and Os-doped YbFO powders can be seen in [15].

Figure 1 represents the surface topography of YbFO and Os-doped YbFO pellets. The existence of agglomeration can be seen in Fig. 1 for all studied samples. It should also be stated that the examined samples exhibit the voids structure on the surface, which is consistent with their cross-sectional SEM images [15]. Such void structures underline the scrutinized samples display porosity nature.

The oxidation levels of Fe and Os have been discussed in detail in our previous study [15]. Our XPS analysis, presented in [15], has revealed the valance states of Fe as 2+ and 3+. Moreover, the valance states of Os have been realized as 0 and 4+. It has been noted that the presence of Fe 2+ has increased as the dopant level of Os is furthered. Such increase in the Fe 2+ might be connected to (i) the oxygen vacancies, which are initiated because of high sintering temperature, (ii) holding the charge balance owing to the presence Os atom in the structure [15 and references in it].

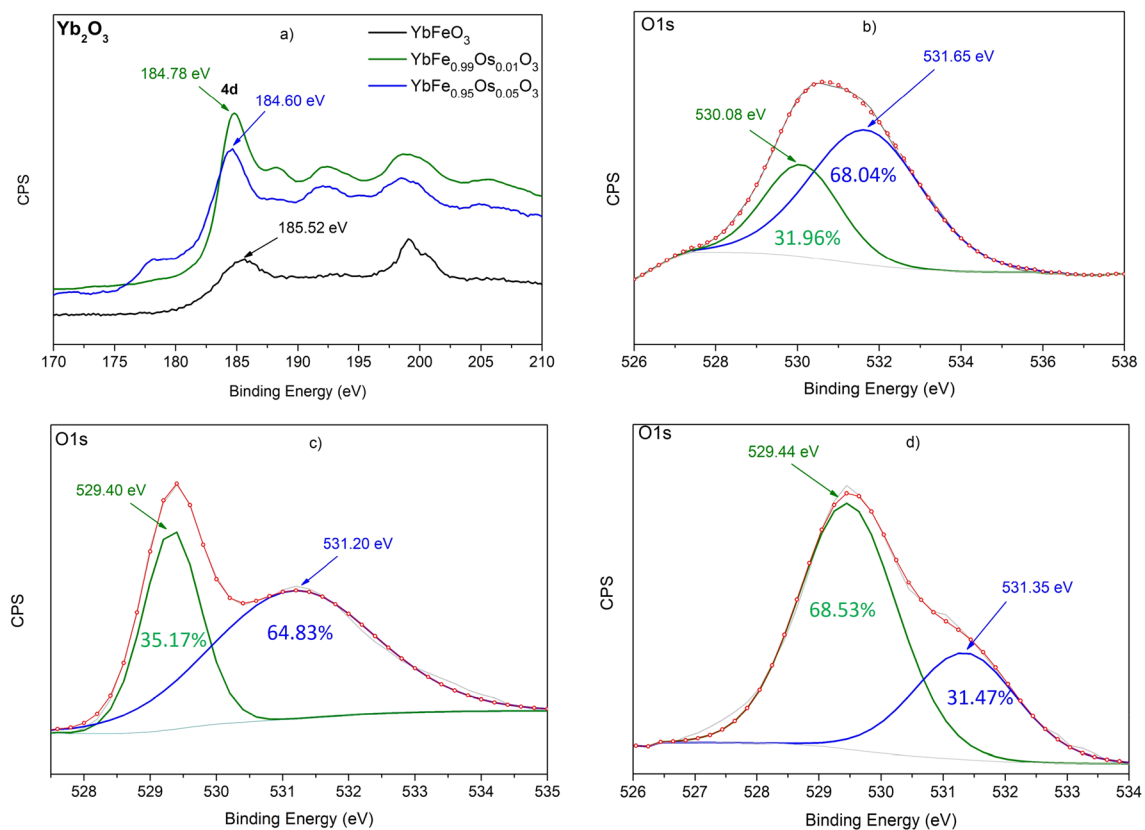


Fig. 2 XPS examination of YbFO and Os-doped YbFO composites: **a** Yb 4d spectrum for studied samples, O 1s spectrum of **b** YbFO, **c** 1 mol% Os and **d** 5 mol% Os-doped YbFO compounds

In this manuscript, the valence states of Yb and O elements are provided. Figure 2a represents the doublet peaks of Yb, which are appearing around 184 eV and 200 eV. These doublet peaks exhibit that Yb has 3+ oxidation state and those binding energies are close the literature values [19]. Figure 2b–d show the O 1s peak for the undoped, 1 mol and 5 mol% Os-doped samples, respectively. From the figures, it is seen that O 1s peak can be separated into two peaks, one is around 530 eV that is associated to the lattice oxygen and other peak becomes visible about 531.3 eV, which is attributed to the oxygen deficiency/vacancy in the compound [20]. The Gaussian fitting unveils that the percentage of oxygen vacancies diminishes from 68.04 to 31.47% as the Os substitution is accelerated. In other words, the Os-doped samples exhibit less oxygen vacancies than the undoped YbFO sample.

Figure 3 represents the frequency dependence of loss-tan(δ), $\tan(\delta) = \varepsilon''/\varepsilon'$ here ε'' and ε' are the imaginary and real part of dielectric function, respectively, between -100°C and 100°C with 20°C increasing step. The loss-tangent is an important parameter of a dielectric material because it quantifies the dissipation of electromagnetic energy at different

applied frequencies. Figure 3a displays the evolution of loss-tan(δ) values of the undoped YbFO with respect to applied frequency at various operating temperatures. It seems that the loss-tan(δ) has a maximum value (peak, which demonstrates the relaxation and represented by f_1) around 10^3 Hz at -100°C and -80°C and it lowers as the applied frequency is further boosted. On the other hand, when the temperature is in the range of $-60^\circ\text{C} \leq T \leq 20^\circ\text{C}$, the initiation of two peaks become visible (they are denoted by f_1 and f_2). One peak appears at low frequency and other one shows up at higher frequency. Additionally, those peaks migrate to the advanced frequency as the temperature increases. Such behavior emphasizes the relaxation process is affected by temperature [21, 22]. Yet, when the temperature is further advanced, $T \geq 40^\circ\text{C}$, three relaxation peaks, one at (shown by f_3) low and other two at high frequencies (f_1 and f_2 , respectively), become eminent. It should be noted that the relaxation peaks shift to the higher frequencies as temperature goes up, Fig. 3a. The progress of loss-tan(δ) values of 1 mol% Os-doped YbFO is denoted in Fig. 3b as function of frequency and temperature. The initiation of two small shoulders is seen at low and higher frequencies at -100°C and -80°C (f_1 and f_2). When the operating temperature is

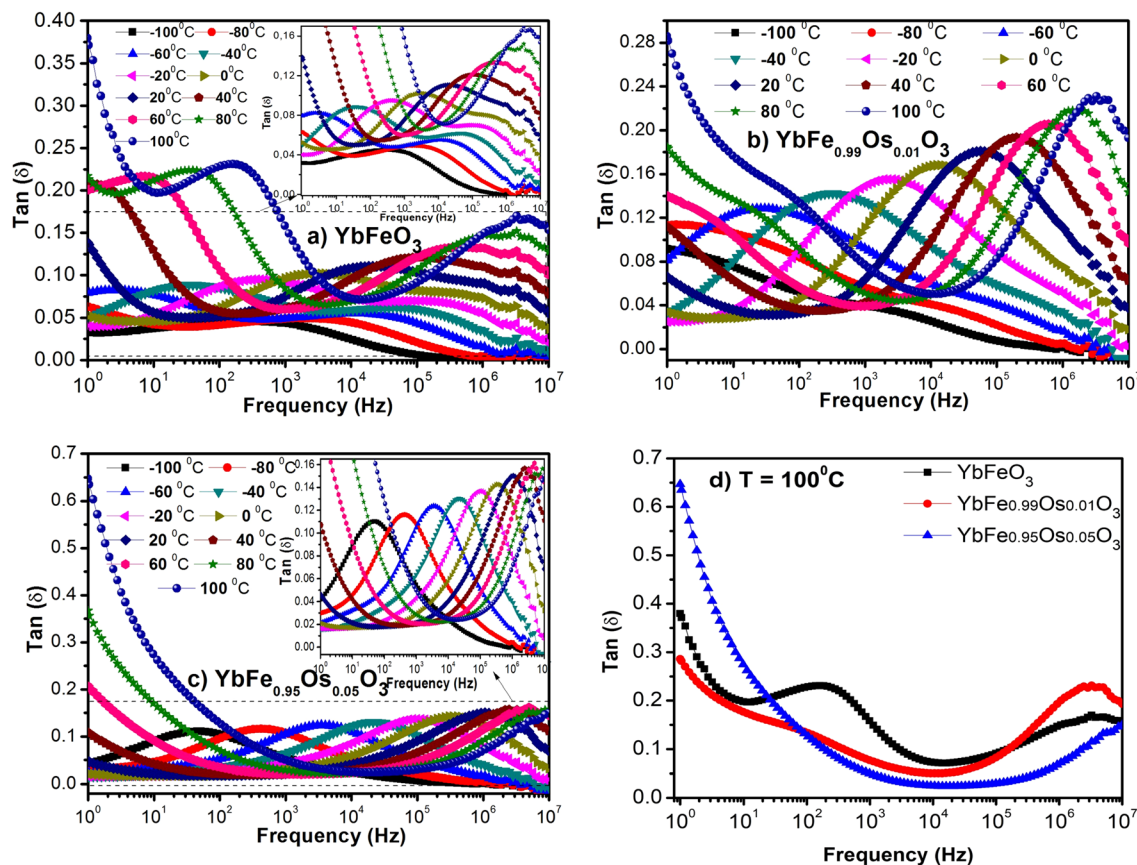


Fig. 3 The variation of $\tan(\delta)$ with respect to frequency and temperature for **a** YbFO, **b** 1% Os and **c** 5% Os-doped YbFO specimens **d** represents the comparison of $\tan(\delta)$ at 100°C

in the range of $-60\text{ }^{\circ}\text{C} \leq T \leq 0\text{ }^{\circ}\text{C}$, one big relaxation peak (at low frequency region, demonstrated by f_1) and small shoulder (at high frequency region, displayed by f_2) can be observed. At $20\text{ }^{\circ}\text{C}$ and $40\text{ }^{\circ}\text{C}$ temperatures, only one visible relaxation peak is noted in the same figure. On the other hand, at higher temperatures, $60\text{ }^{\circ}\text{C}$, $80\text{ }^{\circ}\text{C}$ and $100\text{ }^{\circ}\text{C}$, one big peak (at high frequency, exhibited by f_2) and one small shoulder (at low frequency, denoted by f_3) are noticeable, Fig. 3b. It is also noted that the peaks are moving to the higher frequency values as the operating temperature is further accelerated. Nevertheless, in the case of 5 mol% Os-substituted sample, we have a different picture, Fig. 3c. While one noticeable relaxation

appears in the range of $-100\text{ }^{\circ}\text{C} \leq T \leq 60\text{ }^{\circ}\text{C}$, no observation of relaxation peak at $T \geq 80\text{ }^{\circ}\text{C}$ due to the instrument limitation. Figure 3d compares the loss-tan(δ) values of the studied samples at $100\text{ }^{\circ}\text{C}$. It is seen that at high frequencies, 5 mol% Os-doped sample has lower loss-tan(δ) values. Such low loss-tan(δ) value makes the 5 mol% Os-doped sample a potential material for the future electronic device applications. Because of this potential, the real part of the permittivity of the 5 mol% Os-doped sample at various frequency and temperature are given in Table 1.

As it is noted from Fig. 3, loss-tan(δ) has larger values at low frequencies, which might be initiated due to (i) the impact

Table 1 The real part of the permittivity (or dielectric constant) of the 5 mol% Os-doped sample at different frequency and temperature values

	- 100 °C	- 80 °C	- 60 °C	- 40 °C	- 20 °C	0 °C	20 °C	40 °C	60 °C	80 °C	100 °C
10 MHz	27.44	27.60	27.81	27.98	28.25	28.78	29.76	31.46	34.02	37.17	40.38
1 MHz	27.21	27.37	27.73	28.36	29.61	31.96	35.64	39.69	43.15	45.84	47.85
100 kHz	27.18	27.58	28.67	30.79	34.91	39.79	43.56	46.27	48.17	49.49	50.54
10 kHz	27.66	28.86	32.03	37.72	42.58	45.68	47.80	49.21	50.28	51.30	52.27
1 kHz	28.94	32.10	38.73	43.45	46.37	48.35	49.60	50.67	51.71	52.76	54.21
100 Hz	32.42	38.75	43.64	46.51	48.57	49.84	50.96	52.04	53.31	55.58	60.02

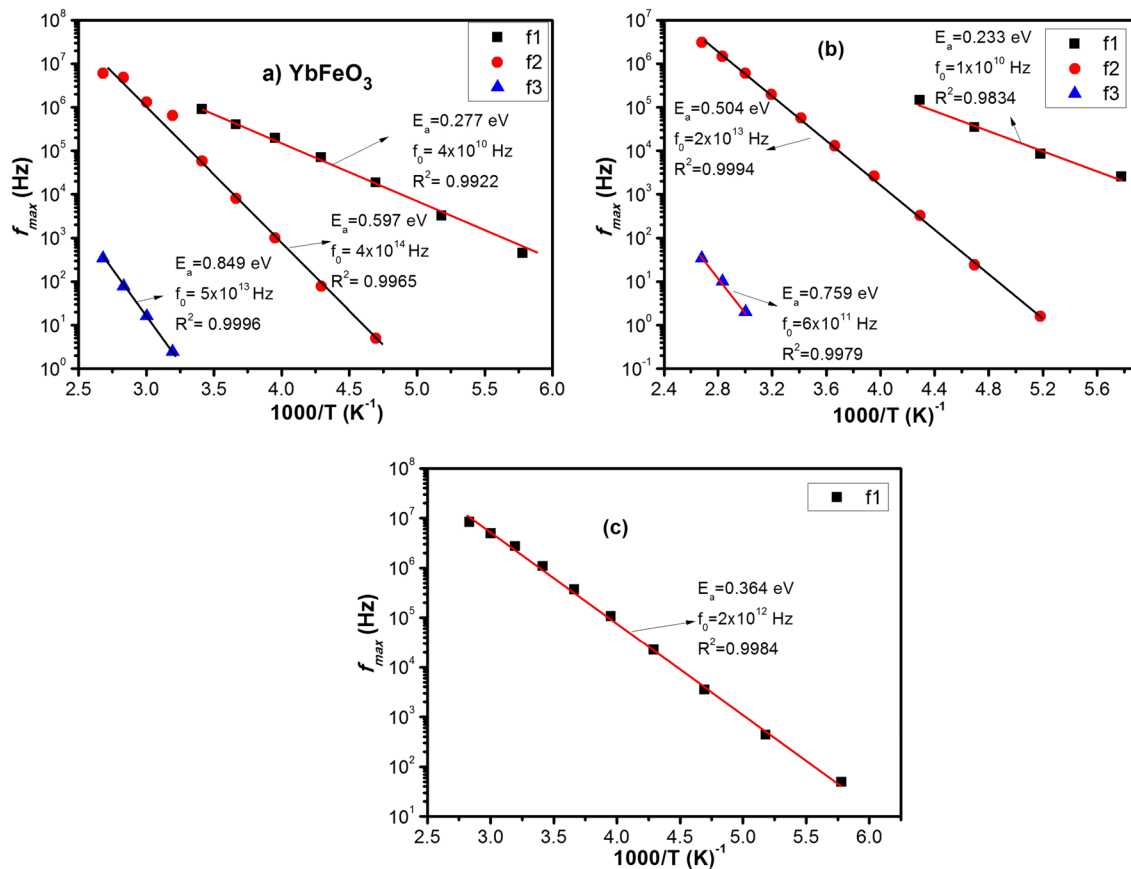


Fig. 4 f_{max} vs. $1000/T$ plots for **a** YbFO, **b** 1 mol% Os-doped and **c** 5 mol% Os-doped YbFO

of interfacial loose and (ii) the presence of grain boundaries that diminish the mobility/migration of electrons between ions. It should be also noticed that as temperature goes up, the loss-tan(δ) values advance. Because such high loss can be connected to charge exchange between Fe^{2+} and Fe^{3+} ions via resistive grain boundary.

As it is mentioned above that the relaxation peaks move toward higher frequencies with operating temperature, which points out the temperature dependency of relaxation peaks. It is shown that such temperature dependency of relaxation peaks can be well described with Arrhenius:

$$f_{\max} = f_0 e^{\left(-\frac{E_a}{k_B T}\right)} \tag{1}$$

here f_{\max} , f_0 , E_a , k_B and T are the max. peak frequency of $\log f$ vs. $\tan(\delta)$ plots, which can be extracted from Fig. 3, frequency dependent pre-exponential factor, activation energy, Boltzmann constant and the absolute temperature, respectively. The Arrhenius relation has been employed to calculate the activation energies of every individual relaxation peaks, which are presented by f_1 , f_2 and f_3 . We have constructed Fig. 4 (f_{\max} vs. $1000/T$) by utilizing f_{\max} values from Fig. 3. It is seen that the undoped YbFO sample has three activation energy, depending on the relaxation type,

Fig. 4a. Here, f_1 , f_2 and f_3 represent the grain boundary, grain, and Maxwell–Wagner (effective at low frequency and high operating temperatures) relaxations, respectively. The obtained activation energies, f_0 and fitting R^2 values of the undoped sample are shown in Fig. 4a. It is seen that subtracted activation energies vary between 277 and 849 meV. The calculated activation energies of 1 mol and 5 mol% Os-substituted samples are shown in Fig. 4b, c, respectively. The activation energies of Os-doped samples vary between 233 and 504 meV depending upon the operating temperature. It can be concluded that the relaxation process taking place in the studied samples are due to oxygen vacancies whose presence has been shown in our XPS Fig. 2b–d. Because the activation energy of single- and double-ionized oxygen vacancies is 300–500 meV and 600–1200 meV, respectively [23, 24].

The impedance spectroscopy technique is employed to study the influence of grain boundary, grain, and electrode on the electrical features [25]. The complex impedance, Z^* , of a material is denoted by [26]:

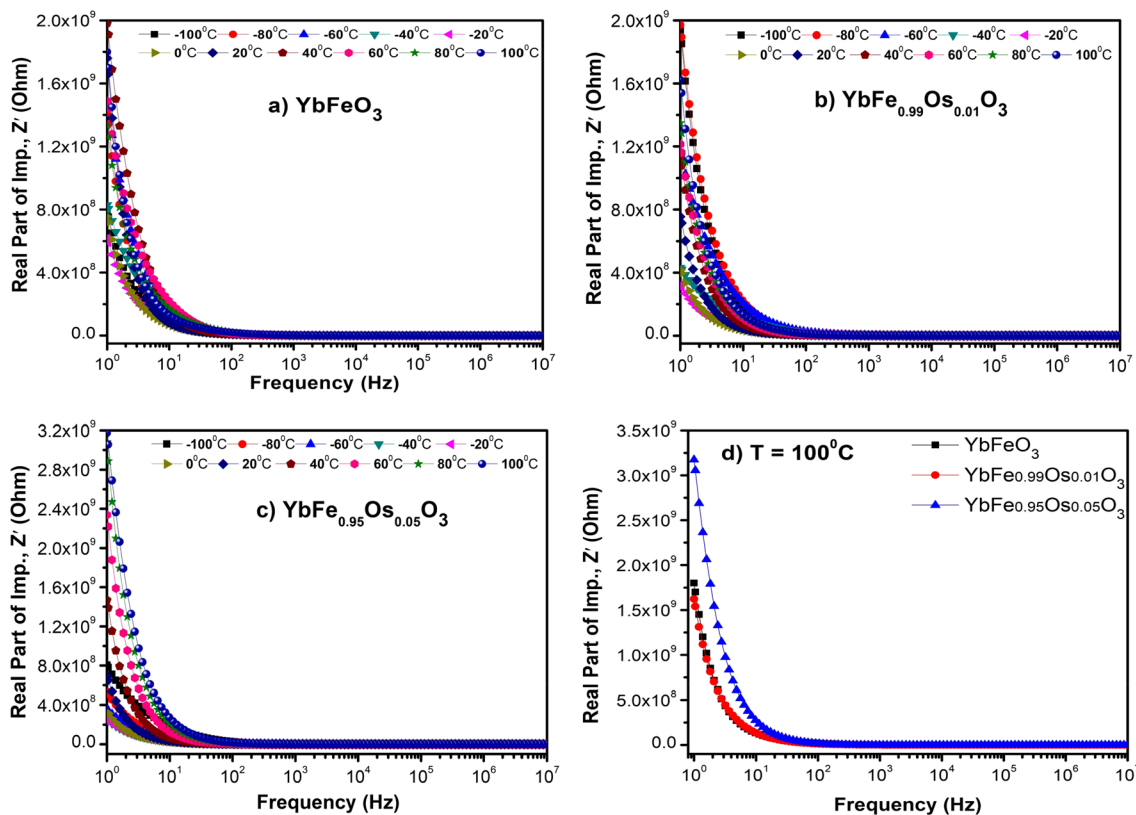


Fig. 5 Variation of real part of the impedance with respect to frequency and temperature for **a** YbFO, **b** 1 mol%, **c** 5 mol% Os-substituted YbFO. **d** The real part of impedance of the studied samples is compared at 100 °C

$$Z^* = Z' - jZ'' = \frac{1}{j2\pi f \epsilon^* C_0} = \frac{\epsilon'' - j\epsilon'}{2\pi f C_0 [(\epsilon')^2 + (\epsilon'')^2]} \quad (2)$$

Here, Z' , Z'' , f , ϵ^* , C_0 are the real and imaginary parts of impedance, frequency, complex dielectric function and empty capacitance of the sample, respectively. The real part of impedance, Z' , of the investigated samples versus frequency at different temperatures is given in Fig. 5 (semi-log scale). It is seen that the Z' values of the undoped and Os-doped YbFO samples diminish as the applied frequency advances until couple of ten hertz at the all operating temperatures, then frequency-independent area is initiated between 10^2 and 10^7 Hz. As it is noted that when the applied frequency goes up the all curves start to overlap, and they form this frequency liberated region in which the energy barrier is reduced [27]. It should also be said that frequency-free region extends as the operating temperature is escalated. Figure 5d compares the Z' values of the investigated compounds at 100 °C. It is seen that the frequency-independent region initiates around 20 Hz for the undoped and 1 mol% Os-doped samples, whereas the same region starts at slightly larger frequency, ~ 35 Hz, for the 5 mol% Os-substituted compound.

The frequency dependency of imaginary part of impedance, Z'' , at various temperatures is given in Fig. 6 (semi-log scale). It is seen that all studied samples exhibit similar behavior: at low frequency region (0–20 Hz) Z'' decreases steeply and becomes frequency-independent, forming frequency-free region, as the frequency is advanced further. Such act might be ascribed to the buildup of space charges at higher frequency area [28]. Furthermore, as the operating temperature is enhanced this region prolongates to the lower frequency region. It should be stated that the formation of any relaxation peak has not been observed in the present compounds because of the instrument limitation.

Figure 7 (semi-log scale) and inset figures (log–log scale) show the resistivity of the studied samples with respect to applied frequency at temperatures between – 100 °C until 100 °C with 20 °C steps. It is noted that the resistivity of samples diminishes with higher frequencies and temperatures. The same figures also represent that the investigated samples do not exhibit the formation of frequency-free region, known as dc resistivity, at the operating frequencies and temperatures. In Fig. 7d, the comparison of resistivity values of the examined samples can be seen at 100 °C. It is seen that the 5 mol% Os-doped sample illustrates the highest

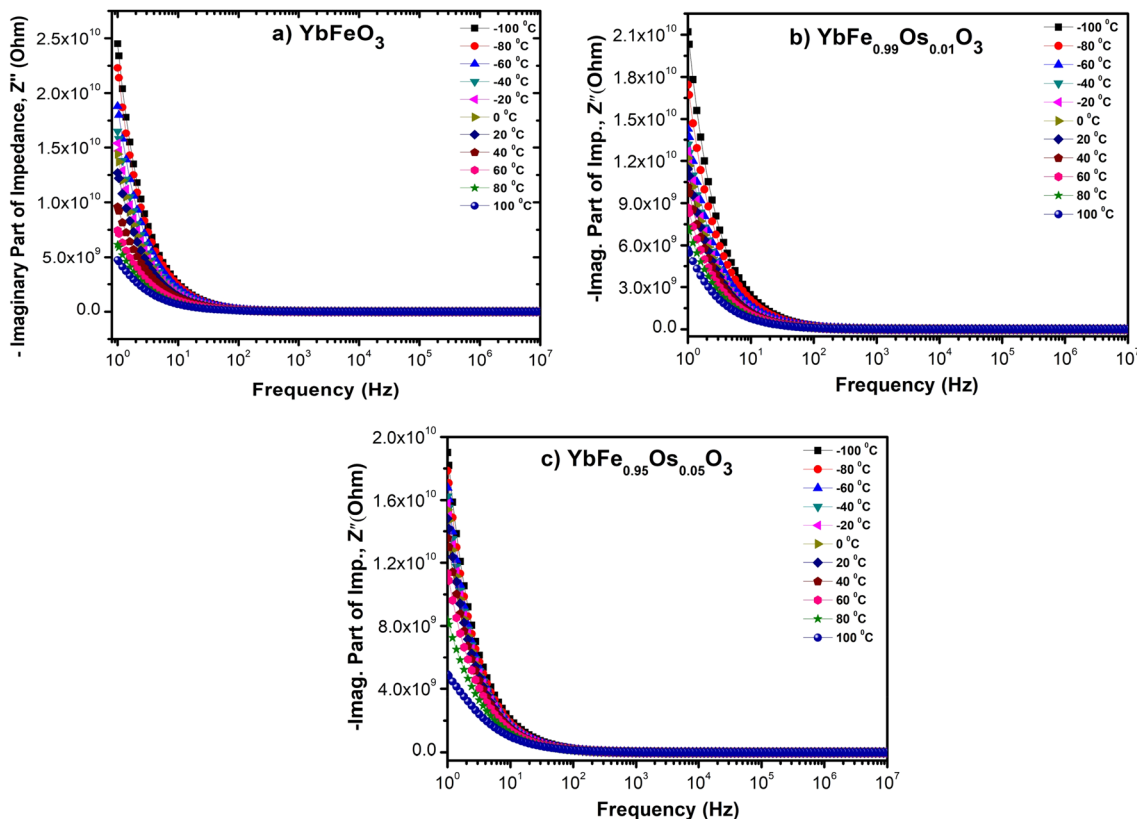


Fig. 6 The imaginary part of impedance variation at various frequencies and temperature values for **a** YbFO, **b** 1 mol% Os and **c** 5 mol% Os-substituted YbFO composites

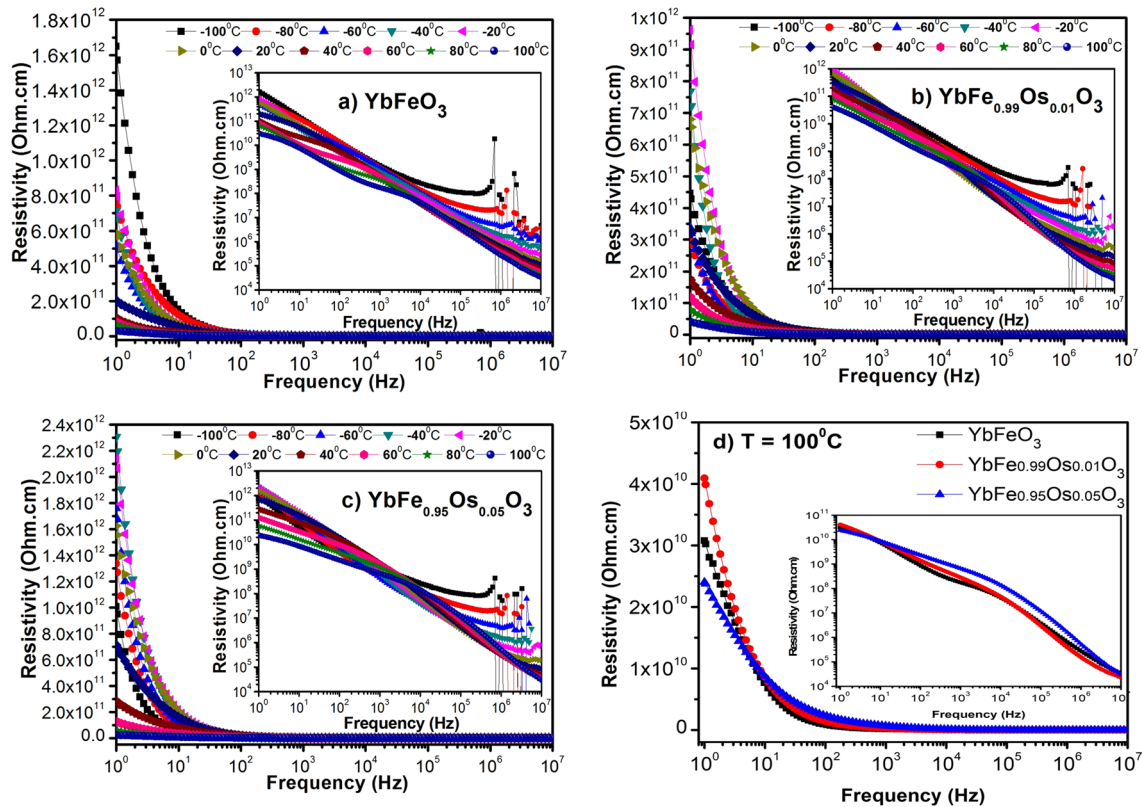


Fig. 7 Resistivity variation at different temperatures for **a** YbFO, **b** 1 mol%, **c** 5 mol % Os-doped YbFO. **d** The comparison resistivities of the investigated samples at 100 °C

resistivity (between 10^2 and 10^6 Hz) among the studied samples. Such high resistivity of 5 mol% Os-doped sample could be related to (i) less oxygen vacancy concentration. Our XPS examination has revealed that the concentration of oxygen vacancies decreases from 68.04% to 31.47% as Os doping ratio is boosted from 0 to 5 mol % [29]. (ii) Os substitution can distort the crystal structure of YbFO owing to ionic radii difference between Fe and Os and such lattice distortion might lead to the formation of potential well trapping the charge carriers and increasing the resistivity [30].

The Raman spectra of the fabricated powders are provided in Fig. 8. In our previous study, we exhibited that YbFeO₃ has orthorhombic *Pnma* structure [15]. Kroumova et al., have shown that orthorhombic *Pnma* structure has 24 Raman active vibrational modes [31], which are given by $\Gamma_{RA} = 7A_g + 5B_{1g} + 7B_{2g} + 5B_{3g}$ relation. The peaks below 200 cm^{-1} are assigned to the displacements of heavy rare-earth ions in the structure. The peaks appear at 269 cm^{-1} , 348 cm^{-1} , 443 cm^{-1} , and 509 cm^{-1} are associated to the excitation of magnetic Fe³⁺ ions [32]. The peak observed at 646 cm^{-1} might be linked to impurity scattering [33] or second-order Raman scattering [34]. It is seen that the peak intensity increases as the Os substitution accelerates. Such increment in the intensity might

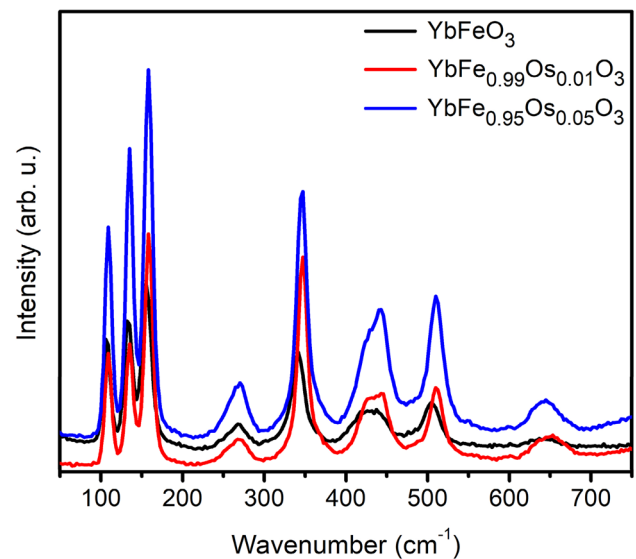


Fig. 8 Raman spectra for YbFe_{1-x}O_xO₃ ($x=0.00, 0.01$ and 0.05) samples

be connected to (i) the variation of grain size owing to Os dopant (Our previous XRD studies have shown that the grain size of YbFO increases from 43 to 53 nm with Os

dopant [15]) and (ii) oxygen vacancies. In addition to that, a small shift to the higher wavenumbers can be noticed as the Os doping level is advanced. Such shift in the spectrum could be ascribed to the structural disorder initiated by Os substitution.

The Kubelka–Munk technique has been employed to determine the optical band gap of powder samples or opaque films in the literature [35]. In this model, the data of diffuse reflectance (R) spectrum are utilized. For this, R spectra of all the obtained films were measured by taking a BaSO_4 powder as a reference, at room temperatures. The optical band gap (E_g) is identified via the following relation [35]:

$$\left(\frac{F(R)h\nu}{t}\right)^2 = A(h\nu - E_g) \quad (3)$$

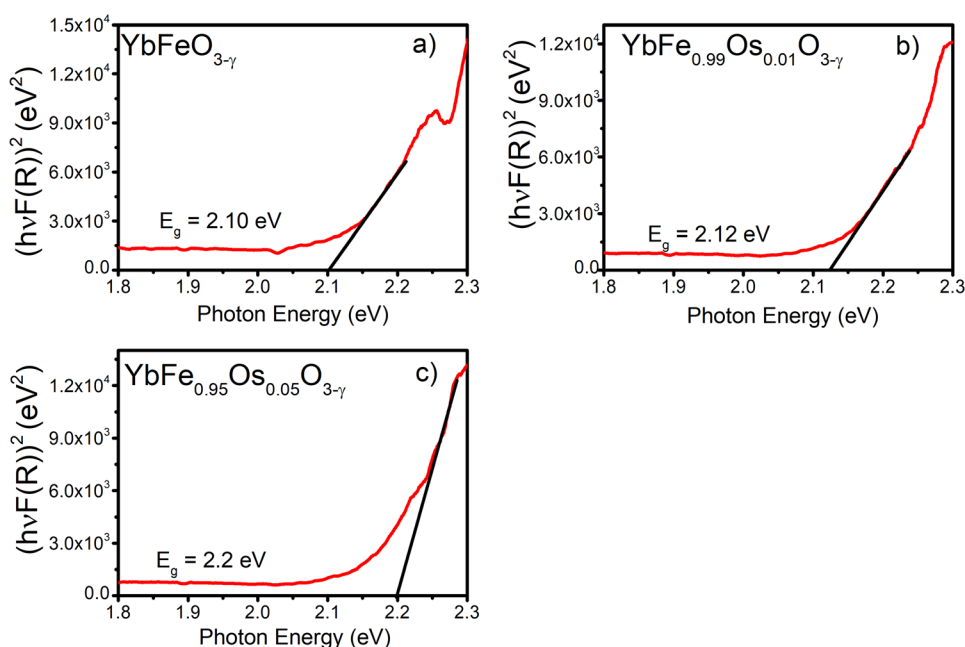
Here, $F(R)$, $h\nu$, t and A are Kubelka–Munk function ($F(R) = (1 - R)^2/2R$), the photon energy, the film thickness and a constant, respectively. The E_g values of the obtained films estimated from the variation of the $(F(R)h\nu)^2$ with $h\nu$ are shown in Fig. 9. As it is noted, the E_g values have been extracted via the extrapolation of the linear portion of the curves. It can be noticed that the optical band gap of YbFO slightly broadens, from 2.10 to 2.2 eV, as the Os dopant level increases. The possible augmentation of the band gap might be associated to (i) band gap tailing due to distribution of impurities/dislocations in the material. Particularly, band gap tailing is employed in polycrystalline samples to define the band spreading [36]. (ii) Moss–Burstein effect [37, 38], occurring when the concentration of carriers dominates the conduction

band edge density of states. Similar results have been obtained in the thin films of Os-doped YbFO [39].

4 Conclusion

The undoped and Os-substituted YbFO powders were prepared via employing solid-state method. The pores structure of obtained powders was unleashed by SEM studies. XPS investigation exhibited that the concentration of oxygen vacancies reduces as the Os doping level advanced to 5 mol%. The loss-tan(δ) values of the studied samples were compared at 100 °C and it was demonstrated the 5 mol% Os-substituted compound holds the lowest loss-tan(δ) values. It was shown that at low frequencies, the loss-tan(δ) has the highest values and such a behavior could be connected to (i) the influence of interfacial loose and (ii) the existence of grain boundaries that lessen the mobility/migration of electrons between ions. Furthermore, it was noted that the loss-tan(δ) values rise with the boosting operating temperature. The activation energies of investigated samples were subtracted from loss-tan(δ) with respect to applied frequency plots via utilizing Arrhenius relation. It turned out that oxygen vacancies dominate the relaxation process. In other words, the relaxation process occurs in the examined specimens are owing to oxygen vacancies because the extracted relaxation energies are close to the relaxation energies of oxygen vacancies in the literature. The impedance and resistivity studies underlined that 5 mol% Os-doped compound has higher resistivity among other samples. Raman investigation exhibited that the obtained compounds have similar space group. The present investigation has laid down that

Fig. 9 Kubelka–Munk plots of the $\text{YbFe}_{1-x}\text{Os}_x\text{O}_3$ ($x=0.00$, 0.01 and 0.05) samples



the electrical features of parent compound, YbFO, can be varied by replacing Fe sites with Os transition elements. It has been shown that the optical band gap of YbFO has increased from 2.1 to 2.2 eV as the Os substitution is elevated to 5%. Such widening in the band gap could be due to (i) band gap tailing and (ii) Moss–Burstein effect. The loss-tan(δ) vs. frequency results at various temperature showed that the YbFO and Os-doped YbFO compound could be a potential materials for the future electronic device applications due to the highly low dielectric loss.

Acknowledgements This work was supported by The Scientific and Technological Research Council of Turkey (TUBITAK) through Grant No: 116F025. We acknowledge CEITEC Nano Research Infrastructure supported by MEYS CR (LM 2018110).

References

- M.A. Ahmed, S.I. El-Dek, Optimizing the physical characterizations of orthoferrites to be used as pressure and gamma sensor. *Mater. Lett.* **60**, 1437–1446 (2006)
- L. Li, X. Wang, Y. Lan, W. Gu, S. Zhang, Synthesis, photocatalytic and electrocatalytic activities of wormlike GdFeO₃ nanoparticles by a glycol-assisted sol-gel process. *Ind. Eng. Chem. Res.* **52**, 9130–9136 (2013)
- H.J. Zhao, Y. Yang, W. Ren, A.-J. Mao, X.M. Chen, L. Bellaiche, Creating multiferroics with large tunable electrical polarization from paraelectric rare-earth orthoferrites. *J. Phys. Condens. Mater.* **26**, 472201 (2014)
- A. Stroppa, M. Marsman, G. Kresse, S. Picozy, The multiferroic phase of DyFeO₃: an ab initio study. *New J. Phys.* **12**, 093026 (2010)
- K.F. Wang, J.M. Liu, Z.F. Ren, Multiferroicity: the coupling between magnetic and polarization orders. *Adv. Phys.* **58**, 321 (2009)
- J.-H. Lee, Y.K. Jeong, J.H. Park, M.-A. Oak, H.M. Jang, J.Y. Son, J.F. Scott, Spin-canting-induced improper ferroelectricity and spontaneous magnetization reversal in SmFeO₃. *Phys. Rev. Lett.* **107**, 117201 (2011)
- Z. Zhou, L. Guo, H. Yang, Q. Liu, F. Ye, Hydrothermal synthesis and magnetic properties of multiferroic rare-earth orthoferrites. *J. Alloy. Compd.* **583**, 21–31 (2014)
- A.A. Bossak, I.E. Graboy, O.Y. Gorbenko, A.R. Kaul, M.S. Kartavtseva, V.L. Svetchnikov, H.W. Zandbergen, XRD and HREM studies of epitaxially stabilized hexagonal orthoferrites RFeO₃ (R = Eu–Lu). *Chem. Mater.* **16**, 1751–1755 (2004)
- M.S.V. Kumar, K. Kuribayashi, K. Kitazono, Effect of oxygen partial pressure on the formation of metastable phases from an undercooled YbFeO₃ melt using an aerodynamic levitator. *J. Am. Ceram. Soc.* **92**, 903–910 (2009)
- H. Iida, T. Koizumi, Y. Uesu, K. Kohn, N. Ikeda, S. Mori, R. Haumont, P.E. Janolin, J.M. Kiat, M. Fukunaga, Y. Noda, Ferroelectricity and ferrimagnetism of hexagonal YbFeO₃ thin films. *J. Phys. Soc. Jpn.* **81**, 024719 (2012)
- H. Iida, T. Koizumi, Y. Uesu, Physical properties of new multiferroic hexagonal YbFeO₃ thin film. *Phase Transit.* **84**(9–10), 747–752 (2011)
- Y.K. Jeong, J.-H. Lee, S.-J. Ahn, S.-W. Song, H.M. Jang, H. Choi, J.F. Scott, Structurally tailored hexagonal ferroelectricity and multiferroism in epitaxial YbFeO₃ thin-film heterostructures. *J. Am. Chem. Soc.* **134**, 1450–1453 (2012)
- O. Polat, M. Coskun, F.M. Coskun, B. Zengin Kurt, Z. Durmus, Y. Caglar, M. Caglar, A. Turut, Electrical characterization of Ir doped rare-earth orthoferrite YbFeO₃. *J. Alloy. Compd.* **787**, 1212–1224 (2019)
- M. Coskun, O. Polat, F.M. Coskun, B. Zengin Kurt, Z. Durmus, M. Caglar, A. Turut, The impact of Ir doping on the electrical properties of YbFe_{1-x}Ir_xO₃ perovskite-oxide compounds. *J. Mater. Sci Mater. Electron.* **31**, 1731 (2020)
- O. Polat, M. Coskun, R. Kalousek, J. Zlamal, B. Zengin Kurt, Y. Caglar, M. Caglar, A. Turut, Frequency and temperature-dependent electric modulus spectroscopy of Os doped YbFeO_{3-δ} structure. *J. Phys. Condens. Matter* **32**, 065701 (2020)
- O. Polat, M. Coskun, F.M. Coskun, J. Zlamal, B.Z. Kurt, Z. Durmus, M. Caglar, A. Turut, Co doped YbFeO₃: exploring the electrical properties via tuning the doping level. *Ionics* **25**, 4013–4029 (2019)
- O. Polat, M. Caglar, F.M. Coskun, M. Coskun, Y. Caglar, A. Turut, An investigation of the optical properties of YbFe_{1-x}Ir_xO_{3-δ} (x=0, 0.01 and 0.10) orthoferrite films. *Vacuum* **173**, 109124 (2020)
- O. Polat, M. Caglar, F.M. Coskun, M. Coskun, Y. Caglar, A. Turut, An experimental investigation: the impact of cobalt doping on optical properties of YbFeO_{3-δ} thin film. *Mater. Res. Bull.* **119**, 110567 (2019)
- SCh. Sarma, U. Subbarao, Y. Khulbe, R. Jana, S.C. Peter, Are we underrating rare-earth as an electrocatalyst? The effect of their substitution in palladium nanoparticles enhances the activity towards ethanol oxidation reaction. *J. Mater. Chem. A* **5**, 23369–23381 (2017)
- N. Paunovic, Z.D. Mitrovic, R. Scurtu, S. Askrabic, M. Prekajski, B. Matovic, Z.V. Popovic, Suppression of inherent ferromagnetism in Pr-doped CeO₂ nanocrystals. *Nanoscale* **4**, 5469–5476 (2012)
- S. Pattanayak, B.N. Parida, P.R. Das, R.N.P. Choudhary, Impedance spectroscopy of Gd-doped BiFeO₃ multiferroics. *Appl. Phys. A* **112**, 387 (2013)
- A.K. Jonscher, The ‘universal’ dielectric response. *Nature* **267**, 673 (1977)
- A.P. Barranco, J.D.S. Guerra, R.L. Noda, E.B. Araujo, Ionized oxygen vacancy-related electrical conductivity in (Pb_{1-x}La_x)(Zr_{0.90}Ti_{0.10})_{1-x/4}O₃ ceramics. *J. Phys. D Appl. Phys.* **41**, 215503 (2008)
- J. Wu, J. Wang, Ferroelectric and impedance behavior of La- and Ti—co doped BiFeO₃ thin films. *J. Am. Ceram. Soc.* **93**, 2795–2803 (2010)
- V. Petrovsky, A. Manohar, F. Dogan, Dielectric constant of particles determined by impedance spectroscopy. *J. Appl. Phys.* **100**, 014102 (2006)
- P.-F. Cheng, J. Song, Q.-P. Wang, S.-T. Li, J.-Y. Li, K.-N. Wu, Fine representation of dielectric properties by impedance spectroscopy. *J. Alloy. Compd.* **740**, 36–41 (2018)
- H.E. Sekrafi, A.B.J. Kharrata, M.A. Wederni, K. Khirouni, N. C.-Boudjadaa, W. Boujelben, Structural, electrical, dielectric properties and conduction mechanism of solgel prepared Pr_{0.75}Bi_{0.05}Sr_{0.1}Ba_{0.1}Mn_{0.98}Ti_{0.02}O₃ compound. *Mater. Res. Bull.* **111**, 329–337 (2019)
- A.R. James, K. Srinivas, Low temperature fabrication and impedance spectroscopy of PMN-PT ceramics. *Mater. Res. Bull.* **34**, 1301 (1999)
- A. Kalabukhov, R. Gunnarsson, J. Börjesson, E. Olsson, T. Claesson, D. Winkler, Effect of oxygen vacancies in the SrTiO₃ substrate on the electrical properties of the LaAlO₃/SrTiO₃ interface. *Phys. Rev. B* **75**, 121404 (2007)
- A.O.A. Keelani, S. Husain, W. Khan, Temperature dependent dielectric properties and ac conductivity of GdFe_{1-x}MnxO₃ (0

- $\leq x \leq 0.3$) perovskites. *J. Mater. Sci. Mater. Electron.* **30**, 20119–20131 (2019)
31. E. Kroumova, M. Aroyo, J.P. Mato, A. Kirov, C. Capillas, S. Ivantchev, H. Wondratschek, Bilbao crystallographic server: useful databases and tools for phase-transition studies. *Phase Trans.* **76**, 155–170 (2003)
 32. P.S.J. Bharadwaj, S. Kundu, V.S. Kollipara, K.B.R. Varma, Synergistic effect of trivalent (Gd^{3+} , Sm^{3+}) and high-valent (Ti^{4+}) co-doping on antiferromagnetic $YFeO_3$. *RSC Adv.* **10**, 22183–22195 (2020)
 33. N. Koshizuka, S. Ushioda, Inelastic-light-scattering study of magnon softening in $ErFeO_3$. *Phys. Rev. B* **22**, 5394–5399 (1980)
 34. V.B. Podobedov, A. Weber, D.B. Romero, J.P. Rice, H.D. Drew, Effect of structural and magnetic transitions in $La_{1-x}M_xMnO_3$ ($M = Sr, Ca$) single crystals in Raman scattering. *Phys. Rev. B* **58**, 43–46 (1998)
 35. A.B. Murphy, Band-gap determination from diffuse reflectance measurement of semiconductor films, and application to photoelectrochemical water-splitting. *Sol. Energy Mat. Sol. Cells* **91**, 1326–1337 (2007)
 36. C. Rajashree, A.R. Balu, V.S. Nagarethinam, Properties of Cd doped PbS thin films: doping concentration effect. *Surf. Eng.* **31**, 316–321 (2015)
 37. E. Burstein, Anomalous optical absorption limit in InSb. *Phys. Rev.* **93**, 632–633 (1954)
 38. T.S. Moss, The interpretation of the properties of indium antimonide. *Proc. Phys. Soc. Sect. B* **67**, 775–782 (1954)
 39. O. Polat, M. Caglar, F.M. Coskun, D. Sobola, M. Konečný, M. Coskun, Y. Caglar, A. Turut, Examination of optical properties of $YbFeO_3$ films via doping transition element osmium. *Opt. Mater.* **105**, 109911 (2020)

Publisher's Note Springer Nature remains neutral with regard to jurisdictional claims in published maps and institutional affiliations.